Fine-Grain High-Performance Densified Oxide Fibers Produced by Open Ultrafast High-Temperature Sintering

Youmei Wang, Weiwei Qin, Zhao Chen, Zhezhe Deng, Dehua Ma, Yifan Wang, Xiaoqing Wang, Yunguang Yin, Yongshuai Xie, Benxue Liu, Luyi Zhu,* Xinqiang Wang, Guanghui Zhang, and Dong Xu*

The considerable grain growth occurring during the long-term high-temperature sintering of polycrystalline oxide fibers negatively affects their mechanical properties, which highlights the need for alternative sintering methods. Herein, open ultrafast high-temperature sintering (OUHS) in air, characterized by rapid heating/cooling (>10000 K min^{-1}) and a short high-temperature holding time (<10 s), is used to produce 3 mol% yttria-stabilized zirconia continuous fibers with coherent boundaries forming robust connections between fine grains. The tensile strength of these fibers (2.33 GPa on average, sintering temperature = 1673 K) notably exceeds that of their counterparts produced by traditional sintering (1.17 GPa). The effects of pores on fiber mechanical properties are analyzed using experimental and theoretical methods. For a versatility demonstration, OUHS is applied to several types of polycrystalline oxide fibers (HfO_2, Al_2O_3, TiO_2, Y_2O_3, and $La_2Zr_2O_7$), considerably improving their mechanical properties and enabling crystalline phase control, which demonstrates the suitability of this procedure for the development of high-performance materials.

1. Introduction

Interactions between grains and microstructural homogeneities are a prerequisite for ensuring the excellent mechanical properties of structural materials, which are usually achieved using high-or ultrahigh-temperature sintering.[1–3] 1D polycrystalline oxide fibers exhibit the advantages of a large aspect ratio and excellent continuity, thus featuring flexibilities unattainable in ceramic films or sheets and finding numerous applications in thermal protection, catalysis, wave absorption, flexible electronics, and other fields.[4–7] Polycrystalline oxide fibers are typically prepared using the organic precursor method, i.e., by the low-temperature decomposition of organics followed by the high-temperature sintering of the thus produced precursor fibers.[8–14] Such sintering is typically performed in muffle furnaces at heating/cooling rates of <10 K min^{-1}, which results in large grain sizes and may therefore lead to structural collapse or even material property loss.[15,16] The prolonged sintering of some fiber materials leads to the appearance of crystalline phases with poor mechanical properties.[17,18] In contrast, the ultrahigh heating and cooling rates of high-temperature sintering help suppress grain coarsening, pore aggregation, substance diffusion, and volatile loss to improve performance[19–25] and thus enable the fabrication of high-performance ceramics inaccessible by traditional sintering (TS).

Solid-phase sintering is characterized by competition and correlation between grain coarsening and densification. With an increase 0 in sintering temperature, surface diffusion is first activated and this mass transfer process occurs with grain coarsening and necking, which increases the diffusion distance of substances from grain boundaries to pores, making it difficult to densification in this process. Further temperature increases can activate grain boundary and lattice diffusion as the main mass transfer processes, which involve grain growth and ceramic densification. Ultrahigh heating rates enable rapid passage through the surface diffusion temperature zone and thus help avoid grain coarsening and pore tip curvature increasing. The results of modeling and simulation studies suggest that higher heating rates result in smaller increases in the curvature radii of pore tips, enhancing grain boundary diffusion and thus contributing to ceramic densification.[26] For some materials, such as ZnO, Al_2O_3, and 3 mol% yttria-stabilized zirconia (3YSZ), rapid heating increases the densification rate.[27–29] Meanwhile, experiments show that rapid heating helps to inhibit pore agglomeration.[30–31] Numerous sintering methods based on different heating principles have been proposed, including ultrafast high-temperature sintering (rate = 10^3–10^5 K min^{-1}),[32] flash sintering (10^3–10^4 K min^{-1}),[33,34] and spark plasma sintering (10^2–10^3 K min^{-1}).[35,36] However, these methods do not

---

Y. Wang, W. Qin, Z. Deng, D. Ma, Y. Wang, X. Wang, Y. Yin, Y. Xie, B. Liu, L. Zhu, X. Wang, G. Zhang, D. Xu
State Key Laboratory of Crystal Materials
Institute of Crystal Materials
Shandong University
Jinan 250100, China
E-mail: liubenxue@sdu.edu.cn; zhuly@sdu.edu.cn

Z. Chen
University of Science and Technology of China
Hefei 230026, China

The ORCID identification number(s) for the author(s) of this article can be found under https://doi.org/10.1002/adma.202412139

DOI: 10.1002/adma.202412139

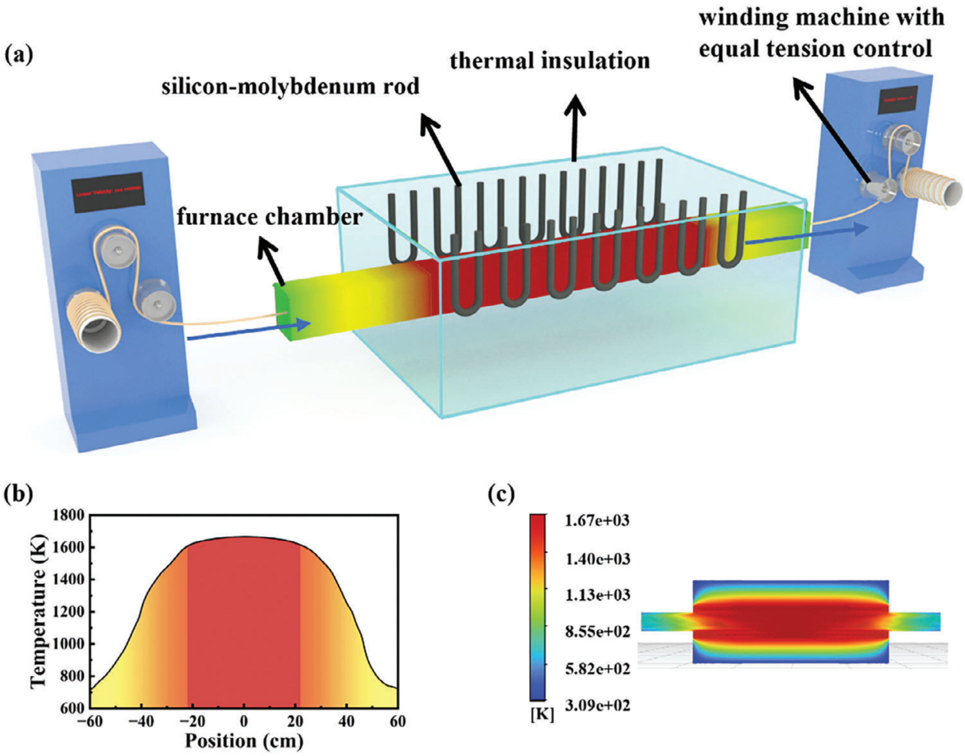

Figure 1. a) Schematic of OUHS equipment. b,c) Simulation of the temperature field of the equipment at a constant temperature of 1673 K.

enable the continuous ultrafast high-temperature sintering of polycrystalline oxide fibers, as they require special atmospheres and confined spaces and impose specific requirements on material shape and electrical properties.

Herein, we used open ultrafast high-temperature sintering (OUHS) to realize continuous sintering at high temperatures (1573–1873 K) and obtain fine-grained densified polycrystalline oxide fibers. 3YSZ continuous fibers, which are advanced ceramic-toughening materials, were used to demonstrate the superior mechanical properties of oxide fibers prepared using OUHS. Presintered 3YSZ continuous fibers, characterized by a low-strength grain interface and low density, were prepared by the organic precursor method[37] involving dry spinning followed by low-temperature heating and subjected to OUHS at different rates of migration through a heated chamber to obtain ultrafine-grained densified polycrystals fibers. Compared with those produced by TS, the 3YSZ continuous fibers processed using OUHS (heating/cooling rate = 10 000 K min^{-1}, holding time at 1673 K = 8 s) exhibited a 65% lower grain size and roughly two times higher tensile strength. The applicability of OUHS to other polycrystalline oxide fibers was verified by analyzing the mechanical properties and crystalline phase compositions of OUHS-produced 3YSZ, TiO_2, HfO_2, Al_2O_3, Y_2O_3, and $La_2Zr_2O_7$ fibers.

2. Results and Discussion

2.1. Schematic of OUHS

Figure 1a presents a schematic of the OUHS equipment, which was insulated using an alumina wrap and contained a heating source (silicon–molybdenum rods) enclosed by a heating chamber with open ends, therefore enabling fiber tension control.

The temperature field of the OUHS equipment was examined using a combination of measurements and simulations (Figure 1b,c; Figure S1, Supporting Information) and was characterized by a high relatively constant temperature within the heating chamber that rapidly decreased outside. The temperature distribution followed a parabolic-like curve with a large slope until the set temperature position was reached (Figure 1b). If the sintering samples migration through the heating chamber at a sufficiently high rate, it could be assumed that the temperature distribution in the heating chamber to reach the target temperature is linearly distributed. By adjusting the time of passage through the heating chamber at a constant speed, we controlled the sample heating/cooling rate and high-temperature holding time. The size of the heating element and heating chamber could be adjusted to regulate the maximum temperature and temperature zone. The employed equipment could deliver a maximum temperature of ≈1873 K, heating/cooling rate of ≈10 000 K min^{-1}, and a high-temperature holding time of <10 s.

Most previously reported ultrahigh-temperature sintering devices relied on ultrafast pulse heating sources to achieve rapid sintering; in contrast, we realized ultrafast sintering by rapidly passing samples through a fixed heating source, which is more suitable for continuous fiber preparation. Unlike other ultrafast sintering methods used to prepare polycrystalline oxide fibers, our technique offers the advantages of (1) ultrafast heating/cooling, (2) insensitivity to material shape and electrical properties, (3) removal of organic precursor–derived carbon in

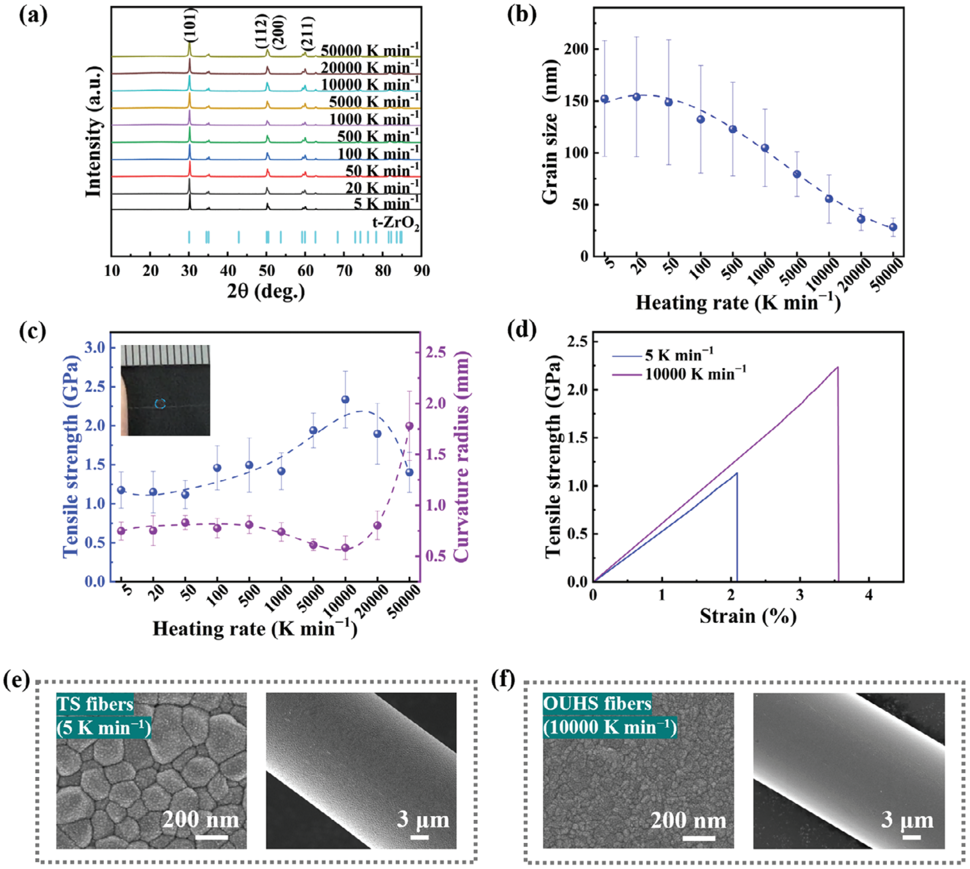

Figure 2. Characteristics of 3YSZ continuous fibers prepared by sintering at 1673 K and different heating rates. Samples prepared at a heating rate of 5 K min^{-1} were sintered using a muffle furnace, and others were sintered using the OUHS equipment. a) XRD patterns, b) grain sizes, c) tensile strengths and curvature radii, d) stress–strain curves. Axial-direction SEM images of fibers prepared by e) traditional sintering (TS) and f) OUHS.

air, (4) possibility of tension loading, and (5) suitability for continuous fiber processing.

2.2. Mechanical Properties of Fibers Prepared Using OUHS

To demonstrate the advantages of OUHS for synthesizing mechanically robust polycrystalline oxide fibers, we examined the microstructural and mechanical properties of crystalline 3YSZ fibers pretreated at 973 K for 60 min and then sintered at 1673 K. Here, we represented different OUHS processes with varying rates of heating, in which the heating, holding, and cooling times remained essentially constant. For comparison, fibers prepared by TS in a muffle furnace at a heating rate of 5 K min^{-1} were characterized. The X-ray diffraction (XRD) patterns of the abovementioned samples showed the predominance of the tetragonal phase (**Figure** 2a) characterized by a high mechanical strength.[17] As the heating rate increased, the (101) peaks broadened, probably because of the concomitant grain size decrease according to the Debye–Scherrer equation (Figure S2, Supporting Information).[38] The fiber grain size was obtained by the analysis of the corresponding scanning electron microscopy (SEM) images and decreased with the increasing OUHS heating rate, which demonstrated the effectiveness of OUHS in minimizing grain growth (Figure 2b). Specifically, a value ≈65% lower than that of TS-prepared fibers was reached at 10 000 K min^{-1}. Hereinafter, fibers prepared by OUHS and TS are referred to as simply OUHS and TS fibers, respectively.

The average tensile strength of OUHS fibers (Figure 2c,d) increased with the increasing heating rate, reaching 2.33 ± 0.36 GPa at 10 000 K min^{-1} and substantially exceeding that of TS fibers (1.17 ± 0.23 GPa) and previously reported values.[39–41] SEM imaging revealed that the OUHS fibers contained tightly bonded nanoscale grains and featured smooth surfaces without cracks and pores (Figure 2e,f), whereas the TS fibers had considerably larger grain sizes and rougher surfaces. A heating rate increase from 10 000 to 20 000 K min^{-1} resulted in decreased strength, mainly because of the shortened high-temperature sintering time and resulting in low densification, high porosity, and abundant surface cracks (Figure S3, Supporting Information). Irrespective of the sintering temperature, the mechanical strength of the OUHS fibers exceeded that of the TS fibers (Figure S4, Supporting Information). The breakage radius was determined as the curvature radius corresponding to the breakage of fibers knotted in a loop and pulled at the ends (inset of Figure 2c). Compared with that of the TS fibers, the breakage radius of the OUHS fibers prepared at 10 000 K min^{-1} was reduced by 50%, which indicated

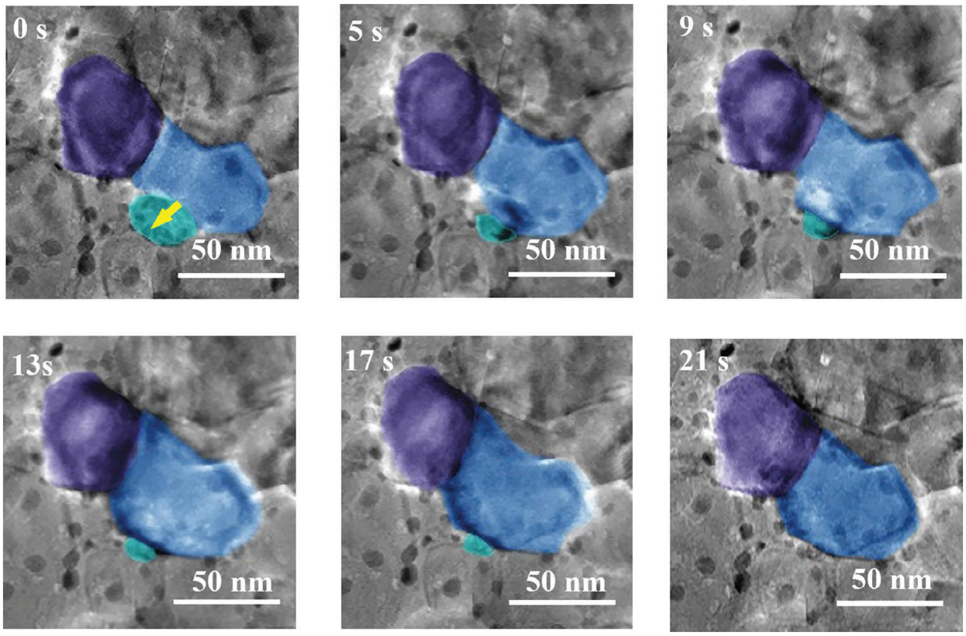

Figure 3. In situ high-angle annular dark-field scanning transmission electron microscopy (HAADF-STEM) image of an OUHS fiber prepared at 1473 K showing the disappearance of a small grain (cyan) due to coalescence growth.

that high-strength and high-tenacity fibers could be obtained at an appropriate heating rate.

Given its relatively disordered atomic arrangement, the grain boundary region features abundant defects and vacancies, which result in grain boundaries being the preferred location of stress concentration under an external force and crack extension.[42–44] Thus, the grain boundary content and uniformity of the grain boundary distribution play important roles in determining fiber strength and toughness. 2D grain models were constructed for fibers with diverse grain sizes, and the grain boundary lengths of these models were determined (Figure S5, Supporting Information). When the diameter of coarse grains reached five times that of fine grains, the boundary length of the fine grains reached ≈5 times that of the coarse grains. Notably, the difference in the grain boundary area was ≈25 times greater when the grains were stacked in 3D. These results indicated that grain size reduction can markedly increase the grain boundary content while ensuring that the fibers reach densification, which can further hinder dislocation motion and reduce stress concentration.

Considering that the grain boundary distribution depends on the grains, we analyzed the grain size uniformity. In the radial fiber direction, when the fiber diameter was sufficiently small, the radial temperature distribution was uniform in high-temperature environments, resulting in OUHS and TS fibers with a high grain size uniformity (Figure S6, Supporting Information). Similarly, in the axial fiber direction, the grain size distribution at different locations on the fiber surface was the same owing to the constant fiber migration velocity (Figure 2e,f). Based on the grain size distribution and statistical results, the grain size distribution of the OUHS fibers was concluded to be more uniform than that of the TS fibers, as the shorter sintering time of the former prevented the abnormal growth of some grains. The improved grain size uniformity resulted in a more uniform grain boundary distribution and thus promoted fiber transfer and uniform stress dispersion. Therefore, the smaller grain size and better uniformity of the OUHS fibers effectively reduced stress concentration at grain boundaries and increased fiber strength and toughness.

2.3. Textural Characteristics and Mechanism of OUHS Fibers

High-temperature environments favor atom movement and diffusion, resulting in fiber densification and grain growth. Thus, understanding the mechanism by which OUHS influences grain refinement and the subsequent strength improvement is crucial for optimizing the preparation of oxide fibers. To characterize grain growth in a high-temperature environment akin to that of the OUHS, we subjected presintered zirconia fibers to focused-ion-beam sectioning and then imaged them by spherical aberration-corrected scanning transmission electron microscopy (STEM) to clarify in situ high-temperature grain growth. A representative boundary between two adjacent grains migrated in the direction of the curvature radius (**Figure 3**, arrow) owing to the difference in the Gibbs free energy, which resulted in smaller grains being incorporated into larger grains to decrease the total energy of the polycrystalline system. The 2D area of the large grains increased from 2095 to 2579 nm^2 before coalescence occurred. Movie S1 (Supporting Information) shows that at a constant temperature of 1473 K, grain growth by coalescence took only 21 s in the selected region.

In ceramics densified by sintering, rapid grain growth in a high-temperature environment mainly occurs in the initial stage, that is, the time derivative of grain size monotonically decreases with time.[45–46] Based on the above experimental results, rapid grain growth in sintered 3YSZ fibers was expected to occur within

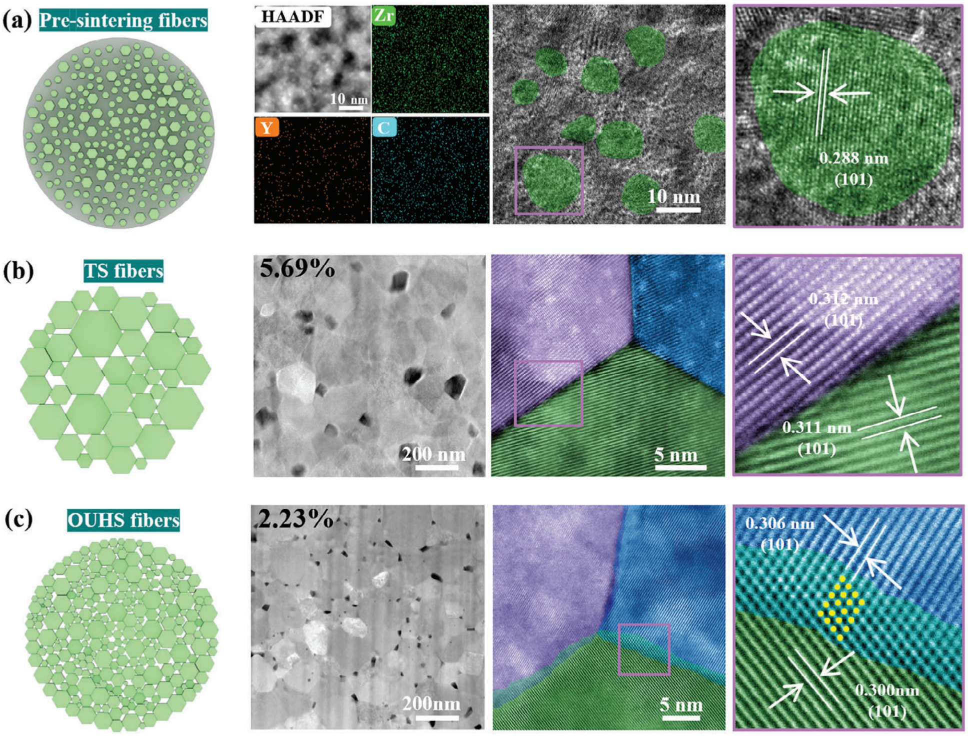

Figure 4. a) Schematic, elemental distributions (determined by energy-dispersive X-ray spectroscopy), and HAADF-STEM images of presintered 3YSZ fibers. Schematic and high-magnification HAADF-STEM images of fibers prepared by b) TS (1673 K, 5 K min^{-1}) and c) OUHS (1673 K, 10 000 K min^{-1}).

<21 s at sintering temperatures above 1473 K. In the case of OUHS, initial coalescence resulted in densification, although further grain coalescence after fiber densification was limited because of the short holding time and fast cooling. The combined results of our and previous studies[26–31] suggest that OUHS can be used to obtain fine-grained dense oxide fibers because of its following advantages. (1) Ultrafast heating enables rapid passage through the surface diffusion temperature zone where densification does not occur, helping avoid grain coarsening and pore tip curvature increasing. (2) When the fiber reaches the high-temperature holding zone, the pore tips with small curvature radii enhance grain boundary diffusion, which reduces the time required for densification. However, this process unavoidable results in grain growth. Thus, a reduction in the time required for densification reduces the time spent in the high-temperature holding zone, leading to minimized grain growth. (3) When the fibers are densified, rapid cooling hinders grain growth.

The presintered fibers had a carbon content of ≈10% of the original value, which prevented ultimate densification. The contrast between the bright and dark regions at different locations in high-angle annular dark-field STEM images due to different mass-thickness contrasts suggested that densification was not achieved (**Figure** 4a). Regarding the internal structure, the presintered fibers consisted of an amorphous phase containing embedded crystalline particles with a grain size of ≈17 nm. As shown in Figure 4a; Figure S7 (Supporting Information), the crystalline particles were identified as tetragonal ZrO_2 with exposed (101) facets. The TS (Figure 4b) and OUHS (Figure 4c) fibers comprised grains and intergranular pores, and the grain size and pores of the latter fibers were markedly smaller than those of the former. The pores within the sintered fibers were counted and sized using the Image J software (Figure S8, Supporting Information). Compared with the TS fibers, the OUHS fibers had a smaller average pore size (25.7 ± 5.2 nm vs 57.2 ± 16.2 nm) and more uniform pore distribution. The results of pore area calculations based on the images in Figure 4b,c show that the pores in the OUHS and TS fibers accounted for 2.23% and 5.69% of the crystalline particle area, respectively. This demonstrated that OUHS effectively promoted densification while suppressing grain growth and pore aggregation.[47]

In terms of the atom arrangement shown in Figure 4b (fourth column), the grain boundaries of the TS fibers were assumed to be formed by grain growth to the point where they met. This coalescence was very fast, as demonstrated in Figure 3, and was likely to terminate in the OUHS fibers because of the short high-temperature holding time and ultrahigh cooling rate. At room temperature, coherent grain boundaries were preserved (Figure 4c, fourth column), which effectively improved intergrain bonding.[48] Considering the sintering process, we speculated that OUHS fibers with smaller grains should exhibit abundant coherent grain boundaries markedly augmenting their mechanical strength, whereas no grain boundaries were detected in the TS fibers.

Subsequently, we explored the influence of pores on the mechanical properties of the OUHS and TS fibers and simulated the corresponding stress distributions using finite element analysis (FEA). During stretching, stress was concentrated at the grain boundaries near the pores, with the magnitude of this concentration increasing with the decreasing number of contact surfaces perpendicular to the external force. The stress in the vicinity of

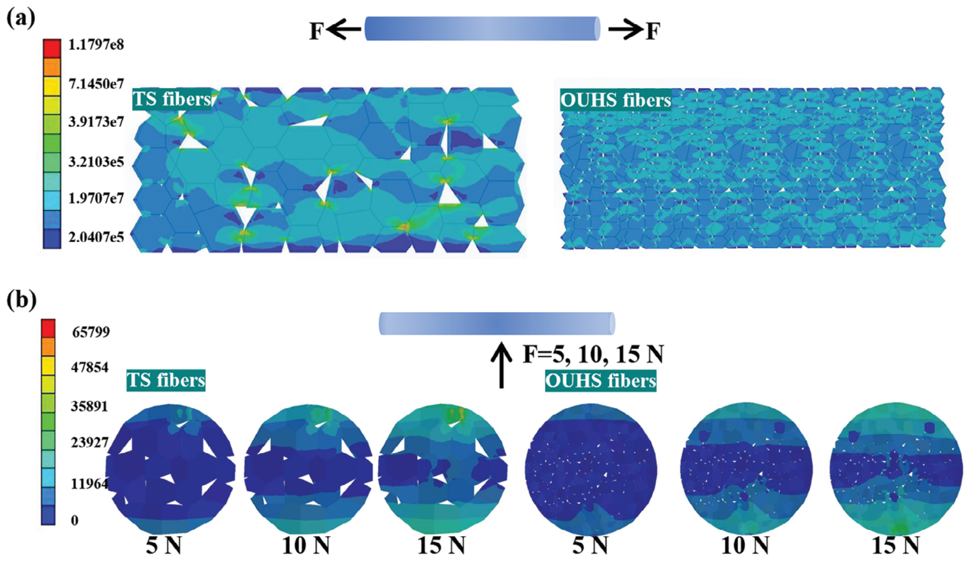

Figure 5. Finite element analysis of the effects of the pores within the sintered fibers on their mechanical properties. Stress distribution of fibers in a) tension and b) bending.

the pores within the TS fibers considerably exceeded that in the OUHS fibers, and the maximum tensile force in the TS fiber model (0.5 N) was smaller than that in the OUHS fiber model (1.5 N). Similarly, 3D models with pores of various sizes were constructed. **Figure** 5b shows the stress distributions in the radial sections of fibers under bending forces of 5, 10, and 15 N, demonstrating a trend similar to that observed for stretching. In summary, the results of FEA indicate that the pores within the fibers play a key role in determining their mechanical strength. The small pores uniformly distributed in the OUHS fibers effectively prevented stress concentration under loading, thus resulting in a stress resistance greater than that observed for fibers with larger pores.

2.4. Universality Demonstration of the OUHS in Preparation of Polycrystalline Oxide Fibers

To verify the applicability of OUHS to the preparation of other polycrystalline oxide fibers, regardless of their constituents and morphology, we used it to prepare common but valuable polycrystalline oxide fibers (3YSZ, HfO_2, Al_2O_3, TiO_2, Y_2O_3, and $La_2Zr_2O_7$)[49–54] and fabricate the corresponding membranes, comparing them with those prepared using TS. The OUHS fiber membranes were more intact and featured fewer breaks, maintaining their morphologies and appearing relatively fluffy (**Figure** 6; Figure S9, Supporting Information), whereas the TS fiber membranes, especially those comprising TiO_2, HfO_2, and Al_2O_3, were broken into pieces. SEM imaging demonstrated that the OUHS fiber membranes exhibited greater integrity with fewer breaks, that is, the TS TiO_2 fibers were not able to maintain their morphologies, unlike the OUHS TiO_2 fibers. The grain sizes of the OUHS fibers were markedly smaller than those of the TS fibers, in line with the above conclusions (Figure S10, Supporting Information). The mechanical properties of the OUHS fiber membranes were considerably improved, which were mainly manifested in their tensile and flexural fatigue resistances (Figures S11 and S12 and Movies S2–S5, Supporting Information). For instance, the OUHS 3YSZ fiber membranes exhibited a notably lower energy loss in the first bend than those produced by TS and were more flexible. This behavior demonstrated the efficiency of OUHS in minimizing grain growth in polycrystalline oxide fibers and realizing excellent mechanical properties.

With the increasing sintering temperature, the thermal vibration of atoms intensifies and enables their rearrangement into the most stable state, which is the root cause of crystalline phase transitions induced by high temperature, e.g., anatase to rutile for TiO_2 and γ-δ-θ-α for Al_2O_3. The presence of various crystalline phases within a given material strongly influences its performance; for example, anatase TiO_2 fibers have better mechanical properties than rutile TiO_2.[55] Regarding Al_2O_3 as a high-temperature thermal insulation material, α-Al_2O_3 has the highest growth rate among all polymorphs, with its explosive grain growth irreversibly damaging the microstructure of oxide ceramics.[56] The relative contents of specific crystalline phases are important factors to consider in material synthesis.

The broad applicability of OUHS and its suitability for tailoring the presence of metastable crystalline phases invaluable for practical applications were demonstrated using TiO_2 and Al_2O_3 fibers. The crystalline phases of the sintered fibers were characterized by XRD and quantified using Rietveld refinement (**Figure** 7; Table S1 and S2, Supporting Information). The Al_2O_3 fibers sintered at 1573 K by OUHS contained the metastable δ phase, which became less dominant with the increasing sintering temperature. In contrast, the Al_2O_3 fibers sintered by TS at 1573, 1673, and 1773 K contained the stable α phase. Additionally, at a sintering temperature of 1773 K, faster heating appeared to facilitate the formation of the metastable δ phase. Similarly, TiO_2 fibers sintered by OUHS at 1573, 1673, and 1773 K contained the anatase phase, which was not accessible by TS. In addition, the exclusive formation of anatase TiO_2 was observed for sintering at 1773 K/30 000 K min^{-1}. Thus, the fibers produced by OUHS

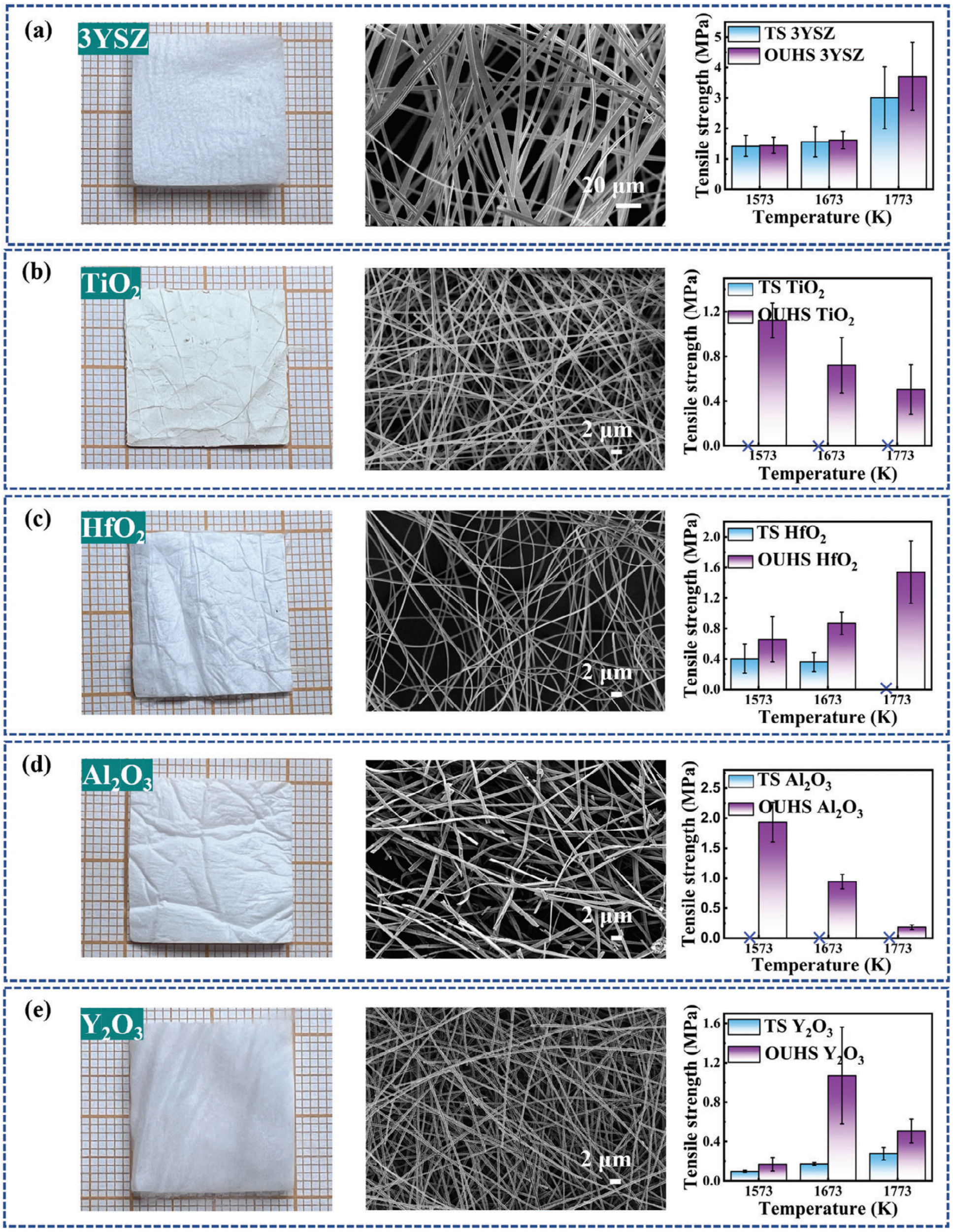

Figure 6. Photographs (first column), SEM images (second column), and tensile strengths (third column) of a) 3YSZ, b) TiO_2, c) HfO_2, d) Al_2O_3 and e) Y_2O_3 fiber membranes prepared by OUHS (10 000 K min^{-1}) and TS (5 K min^{-1}). Data in the first and second columns refer to a sintering temperature of 1773 K.

retained their metastable phases, the content of which could be controlled by adjusting the sintering parameters. This finding demonstrates the high-throughput ability of OUHS to tailor the metastable crystalline phases in oxide fibers.

To examine the advantages of the metastable phase-containing sintered oxide fibers in high-temperature applications, we evaluated their mechanical properties. These fibers should be flexible under ambient conditions because the related practical applications involve folding, cutting, and stretching. Hence, we demonstrated the flexibility of the metastable phase–containing OUHS fibers. Moreover, we tested the pressure elasticity (Figure S13, Supporting Information) of anatase-containing TiO_2 fibers prepared by OUHS at 1573 K/10 000 K min^{-1}, i.e., in an in situ high-temperature environment. The mechanical properties of these fibers were satisfactory, as revealed by resilience in a high-temperature spray gun within 1 min (Movie S6, Supporting Information) and considerable thermal insulation performance at 1592 K (Figure S14, Supporting Information). The spent samples contained both anatase and rutile phases (Figure S15, Supporting Information), which indicated that the metastable anatase gradually transformed into the stable rutile at high temperatures. However, with the prolongation of testing time (e.g., 10 min), the

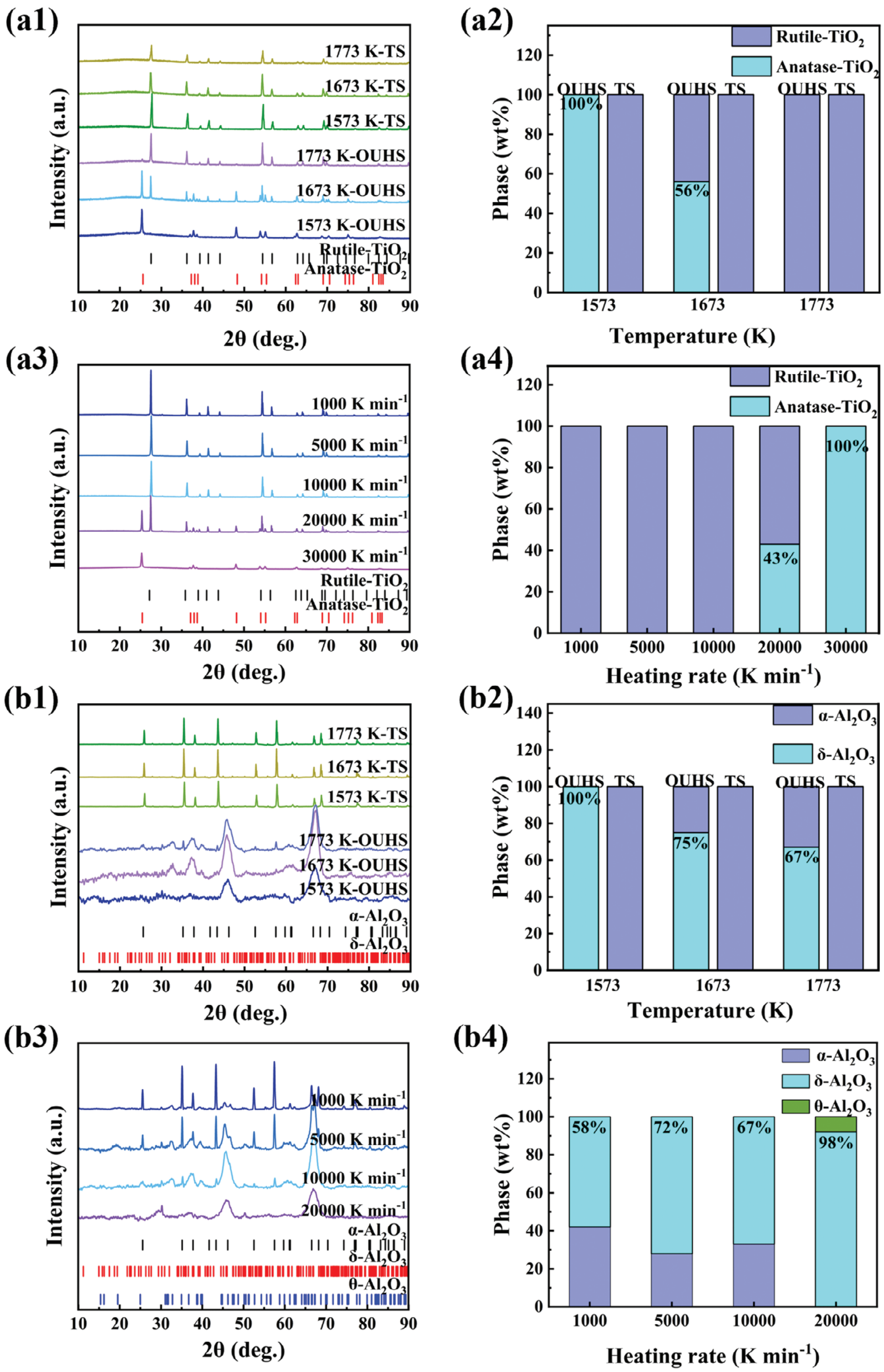

Figure 7. a1) XRD patterns and a2) phase compositions of TiO_2 fibers prepared by OUHS (10 000 K min^{-1}) and TS at different sintering temperatures. a3) XRD patterns and a4) phase compositions of TiO_2 fibers prepared by OUHS at 1773 K and varied heating rates. b1) XRD patterns and b2) phase compositions of Al_2O_3 fibers prepared by OUHS (10 000 K min^{-1}) and TS at varied sintering temperatures. b3) XRD patterns and b4) phase compositions of Al_2O_3 fibers prepared by OUHS at 1773 K and varied heating rates.

resilience disappeared, and a complete transition to rutile was observed (Figure S15, Supporting Information). We hypothesize that the metastable phase–containing oxide fibers prepared by OUHS can meet certain requirements of high-temperature applications because of their excellent mechanical properties under ambient conditions, high thermal insulation performance, and high-temperature mechanical properties that can be retained for a considerable time because of the noninstantaneous nature of their phase transformation. However, due to the phase transition from sub-stable to stable phase will still occur at high temperatures, it is not recommended to be used for a long time at high temperatures, and its specific use time should be explored according to the research of different materials.

3. Conclusion

Ultrafast high-temperature sintering (OUHS) effectively minimized grain coalescence while ensuring densification and strong intergranular bonding, allowing for high grain boundary areas and reducing internal pore aggregation to hinder stress concentration and form fibers with coherent grain boundaries and excellent mechanical properties. The sintering time could be adjusted to control the fiber phase composition and thus achieve the desired properties. Given that OUHS places no limitations on material type, sintering atmosphere, or macroscopic sample shape and allows for the continuity of the sintering process, increased sintering efficiency, and improved material screening, it holds promise for the development of high-performance oxide fiber materials.

4. Experimental Section

Preparation of Presintered 3YSZ Continuous Fibers: A solution of acetylacetone (0.4 mol) and triethylamine (0.6 mol) in methanol (400 mL) was dropwise added to a solution of zirconium chloride octahydrate (0.3 mol) in methanol (500 mL) at 273–277 K upon stirring. After stirring for 24 h at room temperature, the mixture was concentrated, and the residue was treated with tetrahydrofuran (500 mL). The mixture was filtered to remove triethylamine hydrochloride, and the filtrate was concentrated to give polyacetylacetonatozirconium (PAZ). Presintered continuous 3YSZ fibers were prepared using the organic precursor method.[39] PAZ (0.97 mol) and $Y(NO_3)_3 \cdot 6H_2O$ (0.03 mol) were dissolved in ethanol upon continuous stirring for 60 min, and the solution was concentrated under reduced pressure at 310 K using a rotary evaporator to form a transparent spinnable sol with a suitable viscosity. Continuous precursor fibers were obtained using dry spinning, heated to 973 K at a rate of 1 K min^{-1}, and held for 1 h to obtain presintered 3YSZ continuous fibers.

Preparation of Presintered Fiber Membranes: Polyacetylacetonate titanium, polyacetylacetonate hafnium, polyacetylacetonate aluminum, polyacetylacetonate yttrium, or polyacetylacetonate lanthanated zirconium were prepared in a similar manner to PAZ.[50–54] The metal source was dissolved in ethanol, and polyethylene oxide (PEO) was added as a spinning aid. The homogeneous spinning solution was clarified using magnetic stirring. The metal source:ethanol: PEO mass ratio was 1:4:0.01. The spinning voltage was 20 kV, and the receiving distance was 15–30 cm. The precursor fiber membranes were heated to 973 K at 1 K min^{-1} and held for 1 h to obtain presintered fiber membranes.

Characterize: The ANSYS software and 3D global steady-state models were used to simulate the temperature field in the furnace. The models were meshed using the ICEM software, and relevant parameters were then set to iteratively calculate the temperature field until the calculation error converged to $<10^{-5}$. Numerical simulations of the temperature and flow fields were performed using FLUENT's energy equation model, a low Reynolds number turbulence model, and a DO radiation model assuming the system to be in a steady state and the gas to be an incompressible Newtonian fluid satisfying the Boussinesq assumption. Energy in fluids and solids was handled using Equations (1) and (2), respectively.

Energy equations in fluids:

$$\rho C_P \left(u \frac{\partial T}{\partial r} + v \frac{\partial T}{\partial z} \right) = k \left[\frac{1}{r} \frac{\partial}{\partial z} \left(r \frac{\partial T}{\partial r} \right) + \frac{\partial^2 T}{\partial z^2} \right] \tag{1}$$

Energy equations in solids:

$$k \left[\frac{1}{r} \frac{\partial}{\partial r} \left(r \frac{\partial T}{\partial r} \right) + \frac{\partial^2 T}{\partial z^2} \right] - \nabla \bullet q = 0 \tag{2}$$

where T is the temperature, k is the heat transfer coefficient, u and v are flow velocities, C_p is the constant-pressure specific heat capacity of the fluid, ρ is the fluid density, q is the radiative heat flux, and r is the radius.

Presintered 3YSZ continuous fibers were processed for in situ STEM imaging using a focused ion beam (FEI Helios Nanolab G3). The sample was precoated with a carbon/platinum film and transferred to a dissolved heated chip in the focused ion beam chamber. The target area was polished several times using a final ion beam voltage of 2 kV. The local SiN_x support film directly below the target window was completely milled to obtain better imaging conditions. After sample preparation, the heated chips were directly loaded in situ for the experiment. Aberration correction was performed using an FEI Themis transmission electron microscope at an accelerating voltage of 300 kV. Dynamic imaging was performed at 0.5 s frame^{-1} and 1 K s^{-1}.

XRD patterns were acquired using a Rigaku Minifex-600 diffractometer using a step size of 0.02° in the 10–90° range. Quantitative analysis was performed according to the Rietveld method using the GSAS-EXPGUI software package. Standard crystallographic information files (CIFs) for rutile TiO_2, anatase TiO_2, α-Al_2O_3, δ-Al_2O_3, and θ-Al_2O_3 were taken from the American Mineralogist Crystal Structure Database.[57–59] A Hitachi S-4800 scanning electron microscope was used to observe fiber morphologies. The atomic structures of grain boundaries were observed using STEM (JEOL ARM200F). The tensile strengths of the 3YSZ fibers and nanofiber membranes were measured at room temperature using a monofilament tensile testing machine (LLY-06A) at a spacing length of 8 mm and tensile speed of 1 mm min^{-1}. Mechanical behavior was assessed using dynamic mechanical analysis (DMA 850). Infrared images were recorded using a FLIR T540 infrared camera (293–1773 K).

Models for the simulated statistics of grain boundary lengths were developed using Python scripts in ABAQUS. The base was created in ABAQUS. Several points were spread over the base size range, and the Voronoi function was used to create a Voronoi diagram based on these points. The base segmentation in ABAQUS used the generated Voronoi diagram as a sketch to obtain the required model. After the Voronoi function was calculated, the number of edges at the grain boundary was obtained, and the length of the grain boundary was determined from the coordinates of the two endpoints of the edge.

FEA: FEA simulation was performed using the ABAQUS software. The elastic modulus was set to 220 GPa. 2D models based on the internal pore structures of the fibers were established using hexagonal shapes of different sizes as structural primitives. The bound contact was defined between the hexagonal primitives. Similarly, 3D models were constructed for different pore sizes. To demonstrate the dynamic force change during bending, loads of 5, 10, and 15 N were applied to the middle of the fibers.

Supporting Information

Supporting Information is available from the Wiley Online Library or from the author.

Acknowledgements

This work was supported in part by the National Natural Science Foundation of China (grant number 52202090 and 51472144); the Shandong University Young Scholars Program (grant number 2016WLJH27); and the Fundamental Research Funds for the Central Universities (grant number 2082019014).

Conflict of Interest

The authors declare no conflict of interest.

Author Contributions

Youmei Wang: Conceptualization, Formal analysis, Investigation, Writing – original draft. Weiwei Qin: Formal analysis, Validation. Zhao Chen: Formal analysis, Validation. Zhezhe Deng, Dehua Ma, Yifan Wang, and Xiaoqing Wang: Preparation of metal sources for nanofiber membranes. Yunguang Yin and Yongshuai Xie: Formal analysis, Validation. Benxue Liu: Writing – review & editing. Luyi Zhu: Funding acquisition, Supervision, Writing – review & editing. Xinqiang Wang, Guanghui Zhang, and Dong Xu: Supervision.

Data Availability Statement

The data that support the findings of this study are available from the corresponding author upon reasonable request.

Keywords

crystalline phase control, fine grain, mechanical properties, microstructure, open ultrafast high-temperature sintering, oxide ceramic fibers

Received: August 16, 2024
Revised: September 24, 2024
Published online:

---

[1] Z. Wen, Z. Tang, Y. Liu, L. Zhuang, H. Yu, Y. Chu, *Adv. Mater.* **2024**, *36*, 2311870.
[2] C. Liu, Y. Liao, W. Jiao, X. Zhang, N. Wang, J. Yu, Y. T. Liu, B. Ding, *Adv. Mater.* **2023**, *35*, 2304401.
[3] X. Li, Y. Zhang, L. Zhang, S. Xia, Y. Zhao, J. Yan, J. Yu, B. Ding, *Small* **2022**, *18*, 2106500.
[4] X. Chang, Y. Yang, X. Cheng, X. Yin, J. Yu, Y. T. Liu, B. Ding, *Adv. Mater.* **2024**, *36*, 2406055.
[5] Q. Gao, S. Agarwal, A. Greiner, T. Zhang, *Prog. Mater. Sci.* **2023**, *137*, 101139.
[6] Z. Zhang, Y. Zhao, Z. Li, L. Zhang, Z. Liu, Z. Long, Y. Li, Y. Liu, R. Fan, K. Sun, Z. Zhang, *Adv. Compos. Hybrid. Ma.* **2022**, *5*, 513.
[7] X. Chen, A. Selloni, *Chem. Rev.* **2014**, *114*, 9281.
[8] J. Xue, T. Wu, Y. Dai, Y. Xia, *Chem. Rev.* **2019**, *119*, 5298.
[9] T. Zhang, H. Li, Z. Yang, F. Cao, L. Li, H. Chen, H. Liu, K. Xiong, J. Wu, Z. Hong, W. Wang, *Appl. Catal. B Environ. Energy.* **2019**, *247*, 133.
[10] Y. Peng, Y. Xie, Z. Deng, D. Ma, B. Liu, X. Wang, G. Zhang, L. Zhu, *ACS. Appl. Mater. Interfaces.* **2023**, *15*, 14835.
[11] Z. Zhu, X. Zhang, Y. Peng, Z. Guo, Y. Xie, B. Liu, G. Zhang, L. Zhu, X. Wang, Y. Jiang, J. Feng, *Ceram. Int.* **2023**, *49*, 26359.
[12] Y. Xie, Y. Peng, Z. Deng, Z. Zhu, Y. Cheng, D. Ma, L. Zhu, X. Zhang, *Rare. Metals.* **2023**, *42*, 4189.
[13] Z. Deng, Y. Peng, W. W. Qin, B. Liu, G. Zhang, X. Wang, Y. Xie, L. Zhu, D. Xu, *Chem. Eng. J.* **2023**, *475*, 146260.
[14] D. Ma, Y. Wang, L. Wang, Y. Peng, Y. Yin, S. Hou, L. Zhu, X. Wang, B. Liu, G. Zhang, Y. Xie, D. Xu, *ACS. Applied. Nano. Mater.* **2024**, *7*, 15743.
[15] Z. Xu, Y. Liu, Q. Xin, J. Dai, J. Yu, L. Cheng, Y. T. Liu, B. Ding, *Adv. Mater.* **2024**, *36*, 2401299.
[16] J. Guo, S. Fu, Y. Deng, X. Xu, S. Laima, D. Liu, P. Zhang, J. Zhou, H. Zhao, H. Yu, S. Dang, J. Zhang, Y. Zhao, H. Li, X. Duan, *Nature* **2022**, *606*, 909.
[17] Y. Wang, W. Qin, Z. Deng, L. Xu, B. Liu, G. Zhang, X. Wang, L. Zhu, D. Xu, *J. Alloy. Compd.* **2024**, *976*, 173165.
[18] L. Aarik, H. Mändar, A. Tarre, H. Piirsoo, J. Aarik, *Surf. Coat. Tech.* **2022**, *438*, 128409.
[19] M. Hong, Q. Dong, H. Xie, B. C. Clifford, J. Qian, X. Wang, J. Luo, L. Hu, *Acs. Energy. Lett.* **2021**, *6*, 3753.
[20] H. Xie, V. K. Champagne, W. Zhong, B. Clifford, S. Liu, L. Hu, J. C. Zhao, D. R. Clarke, *Adv. Funct. Mater.* **2024**, *34*, 2309978.
[21] M. Kermani, C. Hu, S. Grasso, *Ceram. Int.* **2023**, *49*, 4017.
[22] P. Jiang, G. Du, Y. Shi, F. She, P. Guo, G. Qian, X. Lu, F. Xie, X. Lu, *Chem. Eng. J.* **2023**, *451*, 138771.
[23] D. Zuo, L. Yang, Z. Zou, S. Li, Y. Feng, S. J. Harris, S. Shi, J. Wan, *Adv. Energy. Mater.* **2023**, *13*, 2301540.
[24] M. Guo, Q. Dong, H. Xie, C. Wang, Y. Zhao, X. Wang, W. Zhong, Z. Li, R. Wang, Y. Wang, L. Hao, S. He, G. Chen, W. Xiong, J. Zhao, L. Hu, *Matter* **2022**, *5*, 594.
[25] Z. Lin, X. Zhao, C. Wang, Q. Dong, J. Qian, G. Zhang, A. H. Brozena, X. Wang, S. He, W. Ping, G. Chen, Y. Pei, C. Zheng, B. C. Clifford, M. Hong, Y. Wu, B. Yang, J. Luo, P. Albertus, L. Hu, *Small* **2022**, *18*, 2107951.
[26] E. A. Olevsky, S. Kandukuri, L. Froyen, *J. Appl. Phys.* **2007**, *102*, 114913.
[27] D. Wang, X. Wang, C. Xu, Z. Fu, J. Zhang, *Aip. Adv.* **2020**, *10*, 025223.
[28] M. Chu, M. N. Rahaman, L. C. De Jonghe, R. J. Brook, *J. Am. Ceram. Soc.* **1991**, *74*, 1217.
[29] J. Dong, V. Pouchly, M. Biesuz, V. Tyrpekl, M. Vilémová, M. Kermani, M. Reece, C. Hu, S. Grasso, *Scripta. Mater.* **2021**, *203*, 114076.
[30] C. Liu, R. Chen, Y. Wei, Y. Huang, Z. Zhang, Y. Zhao, T. Fu, C. Hu, X. Huang, X. Zang, *Nano. Energy.* **2023**, *114*, 108634.
[31] D. Kim, C. H. Kim, *J. Am. Ceram. Soc.* **1993**, *76*, 1877.
[32] C. Wang, W. Ping, Q. Bai, H. Cui, R. Hensleigh, R. Wang, A. H. Brozena, Z. Xu, J. Dai, Y. Pei, C. Zheng, G. Pastel, J. Gao, X. Wang, H. Wang, J. C. Zhao, B. Yang, X. R. Zheng, J. Luo, Y. Mo, B. Dunn, L. Hu, *Science* **2020**, *368*, 521.
[33] B. Yoon, V. Avila, I. R. Lavagnini, J. V. Campos, L. M. Jesus, *Adv. Eng. Mater.* **2023**, *25*, 2200731.
[34] A. Gibson, Y. Li, R. S. Bonilla, R. I. Todd, *Acta. Mater.* **2022**, *241*, 118362.
[35] A. M. Laptev, M. Bram, D. Garbiec, J. Räthel, A. van der Laan, Y. Beynet, J. Huber, M. Küster, M. Cologna, O. Guillon, *Adv. Eng. Mater.* **2024**, *26*, 2301391.
[36] O. Guillon, J. Gonzalez Julian, B. Dargatz, T. Kessel, G. Schierning, J. Räthel, M. Herrmann, *Adv. Eng. Mater.* **2014**, *16*, 830.
[37] H. Liu, X. Hou, X. Wang, Y. Wang, D. Xu, C. Wang, W. Du, M. Lü, D. Yuan, *J. Am. Ceram. Soc.* **2004**, *87*, 2237.
[38] A. Pandey, P. Yadav, A. Fahad, P. Kumar, M. K. Singh, *Ceram. Int.* **2024**, *50*, 21417.
[39] L. Wang, B. Liu, Y. Xie, D. Ma, L. Zhu, X. Wang, *J. Am. Ceram. Soc.* **2019**, *102*, 4450.
[40] Y. Abe, T. Kudo, H. Tomioka, T. Gunji, Y. Nagao, T. Misono, *J. Mater. Sci.* **1998**, *33*, 1863.
[41] L. Wang, Y. Xie, D. Ma, L. Zhu, X. Wang, X. Jin, C. Xu, Y. Peng, G. Zhang, D. Xu, *Ceram. Int.* **2019**, *45*, 23037.
[42] T. Tian, Z. Hao, C. Ge, X. Li, S. Peng, C. Jia, *Mater. Sci. Eng. A.* **2020**, *76*, 139007.
[43] W. Mei, Q. Li, X. Chen, *J. Mater. Res. Technol.* **2023**, *23*, 931.

[44] R. Su, J. Chen, H. Chen, Z. Zhang, X. Zhao, Z. Lei, D. Wang, Y. Meng, Z. Zhang, *J. Mater. Sci.* **2023**, *58*, 12775.

[45] Z. Tian, Y. Wang, Z. Zhang, X. Duan, D. Jia, S. Wu, *Mater. Chem. Phys.* **2020**, *248*, 122916.

[46] U. Bansal, V. Singh, K. Brajesh, R. Gupta, A. Garg, *J. Alloy. Compd.* **2020**, *847*, 156499.

[47] S. Y. Gómez, A. L. Da Silva, D. Gouvêa, R. H. R. Castro, D. Hotza, *Mater. Lett.* **2016**, *166*, 196.

[48] X. Ke, J. Ye, Z. Pan, J. Geng, M. F. Besser, D. Qu, A. Caro, J. Marian, R. T. Ott, Y. M. Wang, F. Sansoz, *Nat. Mater.* **2019**, *18*, 1207.

[49] X. Mao, L. Zhao, K. Zhang, Y. Wang, B. Ding, *Nano. Res.* **2022**, *15*, 2592.

[50] Z. Deng, Y. Xie, W. Liu, J. Dong, Y. Peng, Z. Zhu, L. Zhu, G. Zhang, X. Wang, D. Xu, *Ceram. Int.* **2022**, *48*, 16715.

[51] L. Wang, Y. Xie, B. Liu, D. Ma, X. Wang, L. Zhu, X. Jin, Z. Wang, C. Xu, G. Zhang, D. Xu, *Ceram. Int.* **2019**, *45*, 6959.

[52] Y. Xie, L. Wang, B. Liu, L. Zhu, S. Shi, X. Wang, *Mater. Design.* **2018**, *160*, 918.

[53] N. Wang, Y. Xie, J. Lv, J. Zhang, L. Zhu, Z. Jia, X. Tao, *Ceram. Int.* **2022**, *48*, 19460.

[54] W. Liu, Y. S. Xie, Z. Z. Deng, Y. Peng, J. H. Dong, Z. Zhu, D. H. Ma, L. Y. Zhu, G. H. Zhang, X. Q. Wang, *J. Adv. Ceram.* **2022**, *11*, 922.

[55] Y. Song, F. Zhao, Z. Li, Z. Cheng, H. Huang, M. Yang, *Rsc. Adv.* **2021**, *11*, 23901.

[56] Z. Xu, H. Liu, F. Wu, L. Cheng, J. Yu, Y. T. Liu, B. Ding, *Adv. Mater.* **2023**, *35*, 2305336.

[57] P. Von, P. Ewald, C. Hermann, Zeitschrift für Kristallographie, Kristallgeometrie, Kristallphysik, Kristallchemie, Erganzungsband **1931**.

[58] R.-S. Zhou, R. L. Snyder, *Acta. Crystallogr. A* **1991**, *47*, 617.

[59] Y. Repelin, E. Husson, *Mater. Res. Bull* **1990**, *25*, 611.